Dalton Transactions

Accepted Manuscript

This article can be cited before page numbers have been issued, to do this please use: Z. Ren, D. Hu, X. Zhang, D. Liu and C. Wang, *Dalton Trans.*, 2019, DOI: 10.1039/C8DT05150J.

This is an Accepted Manuscript, which has been through the Royal Society of Chemistry peer review process and has been accepted for publication.

Accepted Manuscripts are published online shortly after acceptance, before technical editing, formatting and proof reading. Using this free service, authors can make their results available to the community, in citable form, before we publish the edited article. We will replace this Accepted Manuscript with the edited and formatted Advance Article as soon as it is available.

You can find more information about Accepted Manuscripts in the author guidelines.

Please note that technical editing may introduce minor changes to the text and/or graphics, which may alter content. The journal's standard Terms & Conditions and the ethical guidelines, outlined in our author and reviewer resource centre, still apply. In no event shall the Royal Society of Chemistry be held responsible for any errors or omissions in this Accepted Manuscript or any consequences arising from the use of any information it contains.

ROYAL SOCIETY OF CHEMISTRY

rsc.li/dalton

View Article Online
DOI: 10.1039/C8DT05150J

Journal Name

ARTICLE

Hierarchical Porous Hollow $FeFe(CN)_6$ Nanospheres Wrapped by I-Doped Graphene as Anode Materials for Lithium-ion Batteries

Zhengxin Ren[a], Die Hu[a], Xiannan Zhang[a], Dan Liu[a,b*], Cheng Wang[a*]

Received 00th January 20xx,
Accepted 00th January 20xx

DOI: 10.1039/x0xx00000x

www.rsc.org/

Hierarchical porous hollow $FeFe(CN)_6$ nanospheres were synthesized *via* a facile anisotropic chemical etching route under different temperature. Herein, we integrated these $FeFe(CN)_6$ nanospheres and conductive iodine-doped graphene (IG) into lithium-ion batteries (LIBs) system, $FeFe(CN)_6$@IG. The hollow Prussian-blue type $FeFe(CN)_6$ nanospheres with average particle size of 230 nm are uniformly and tightly encapsulated by IG sheets. As an anode material for LIBs, the fabricated $FeFe(CN)_6$@IG exhibits high specific capacity, excellent rate property, and superior cycling stability. A reversible capacity can be maintained at 709 mAh g^{-1} after 250 cycles at a current density of 1000 mA g^{-1}. Even at a current rate of 2000 mA g^{-1}, the capacity could reach 473 mAh g^{-1}. This facile fabrication strategy may pave the way for constructing high performance Prussian blue-based anode materials for potential application in advanced lithium-ion batteries.

Introduction

Along with the fast development of intelligent robots and electric vehicles, lithium-ion batteries (LIBs), commercialized in 1991, have been widely used as the main energy sources.[1-5] Currently, in LIBs, graphite consists of one of the main electrode materials and encounters limitations in practical applications, especially in electric vehicles, due to its relatively low capacity (372 mAh g^{-1} for LiC_6).[6,7] Energy density of LIBs still need to be further enhanced by improving specific capacity and enlarging working voltage of electrodes, which require high lithiation capability and low polarization capability. Therefore, searching for alternative electrode materials has attracted widespread attention.

Owing to their unique structural features and intriguing properties, hollow micro/nanostructures with diverse hierarchical architectures have gained much attention in many aspects of electrochemistry such as fuel cells, supercapacitors, and LIBs.[8-10] The enhanced electrochemical performance of hollow-structured micro/nanomaterials is attributed to, at least partially, their high surface area and surface to volume ratio. It has been reported that the voids inside hollow nanoparticles can not only provide more space to accommodate volume changes during charge/discharge but also shorten the Li^+ diffusion distance, which lead to less overpotentials and faster reaction kinetics at the electrode surface.[11,12] In the past decade, different types of hollow structures including hollow spheres,[13-15] boxes and micro-/nanotubes[16,17] have been successfully synthesized through different synthetic routes. Among them, hollow spheres with open three-dimensional (3D) architectures have provoked ever-increasing attention, and are the most promising structure for the anode of LIBs. Usually, hollow spheres are prepared from spherical-particle templates, such as silica colloids,[18,19] polystyrene beads,[20-24] inorganic particles,[25-29] followed by the removal of the sacrificial core through calcination or/and solvent etching. These template methods are tedious and poor in reproducible since it is rather difficult to retain the original ordered structures after removing the templates. Recently, Lou et al. reported a structure-induced anisotropic chemical etching method to transform Ni-Co based Prussian-blue analogues (hereafter denoted as PBAs) nanocubes into well-defined cubic NiS nanoframes.[30] Taking advantage of the different chemical stability by location in the nanocubes, complicated hollow structures were formed in the subsequent chemical etching process. With intrinsic structural merits, including 3D hollow, porous structure, small nanoparticle size, and good structural robustness, the as-prepared NiS nanoframes exhibited enhanced electrochemical properties for electrochemical capacitors and hydrogen evolution reaction in an alkaline electrolyte.

Metal-organic frameworks (MOFs), a new class of organic-inorganic hybrid functional materials with high porosity, large surface area and morphology can be easily tuned upon selection of different metal cations and organic bridging ligands.[31-33] As a subclass of MOFs, PBAs with the formula of $M_x[Fe(CN)_6]_y$ (M = Fe, V, Mn, Co, Ni, and Cu) can be synthesized with uniform size, various composition, diverse morphology and architecture.[34-37] The crystal structure of $FeFe(CN)_6$ consists of a three-dimensional network of Fe1-N≡C-Fe2 chains (Figure S1), where the Fe1 are 6-fold coordinated to nitrogen atoms and the Fe2 are octahedrally surrounded by carbon atoms of the CN^- ligands. So far, nanostructured PBAs materials have been extensively

[a] Tianjin Key Laboratory of Advanced Functional Porous Materials and Center for Electron Microscopy, Institute for New Energy Materials & Low-Carbon Technologies, School of Materials Science and Engineering, Tianjin University of Technology, Tianjin 300071(P.R. China)
[b] School of Environment and Civil Engineering, Dongguan University of Technology, NO. 1, Daxue Rd, Songshan Lake, Dongguan, Guangdong 523808 (P. R. China)

Electronic Supplementary Information (ESI) available: [details of any supplementary information available should be included here]. See DOI: 10.1039/x0xx00000x

DOI: 10.1039/C8DT05150J

investigated as precursors/templates to develop new functional nanomaterials with hollow or porous structures. In addition, PBAs themselves have recently exhibited many interesting physicochemical properties, making them be widely applied in cathode or anode materials for LIBs. As cathode materials, nanosized $Fe_4[Fe(CN)_6]_3$ and cubic $FeFe(CN)_6$ deliver reversible capacities of 95 mAh g^{-1} and 138 mAh g^{-1}, respectively.[38] Besides cathode, PBAs can be also used as anode materials for LIBs. $M^{II}{}_3[Co^{III}(CN)_6]_2\ nH_2O$ (M= Co, Mn), a typical PBA, can deliver a reversible capacity of 299.1 mAh g^{-1}, and possess good capacity retention with increased current densities as a result of rapid Li^+ transport through large channels in the open-framework.[39] Even though, these materials suffer from poor cycling stability and low columbic efficiency (<90%), which hinder their commercial applications for LIBs. In fact, these problems are not originated from the intrinsic electrochemistry of the PBAs but are mostly brought about from their low electrical conductivity and rapid capacity fading during the cyclic process. Therefore, PBAs with high electrical conductivity and stability are desired to be used as electrode materials for LIBs.

Graphene has shown many intriguing properties, including superior electrical conductivity, a large surface area, and high chemical stability, and has arisen considerable interest in the field of LIBs.[40] Theoretical calculations have shown that the introduction of heteroatoms (e.g., B, N, P and S) into sp^2-hybridized carbon frameworks in graphene is very effective in improving their electrochemical performance.[41-44] Specifically, iodine-doped graphene (IG) has been reported to increase positive charge density on the graphene through surface charge transfer because of the formation of triiodide (I^{3-}) and pentaiodide (I^{5-}) polyanions.[45] IG possesses a substantial number of electrochemical active sites and enhanced electrical conductivity. These motivate us to combine hollow PBAs nanospheres with IG and investigate their potential applications in LIBs. Herein, hierarchical spheres with hollow interiors composed of $FeFe(CN)_6$ were successfully synthesized via a facile anisotropic chemical etching route under different temperature. Then they were integrated with conductive IG to give $FeFe(CN)_6$@IG. Electrochemical measurements demonstrate that, as a new anode material, $FeFe(CN)_6$@IG composite demonstrates prominent charge/discharge capacities of 715.2/709.5 mA h g^{-1} after 250 cycles at 1000 mA g^{-1} and 449.9/448.0 mA h g^{-1} after 300 cycles at a high current density of 2000 mA g^{-1}.

Experimental

Synthesis of Iodine-Doped Graphene (IG)

Graphene oxide (GO) was prepared from graphite flakes according to the modified Hummers method.[46] Iodine-doped Graphene was prepared following a reported protocol.[45] Briefly, GO and I_2 were first ultrasonically dispersed in ethanol for 60 min. The resultant suspension was spreaded onto a petri dish and dried at 25 °C to form a uniform solid mixture. The mixture was placed into a quartz tube and annealed under argon at 900 °C for 120 min. After cooling down to room temperature naturally in the same atmosphere, IG was obtained.

Synthesis of hierarchical porous hollow $FeFe(CN)_6$ nanospheres with contrasting porosities

Synthesis of $FeFe(CN)_6$-80 nanospheres: 3.00 g PVP and 138.2 mg $K_3[Fe(CN)_6]$ were added to a 100 ml beaker containing 52.5 mL 0.5 M HCl solution under magnetic stirring. After 60 min of stirring, a pale yellow solution was formed and transferred to a 100 ml flask. Then, the flask was placed into a water bath and heated at 80 °C for 24 h under magnetic stirring. The precipitates were collected by centrifugation, washed several times by distilled water and ethanol, and dried at 60 °C for 12 h. $FeFe(CN)_6$-80 nanospheres were obtained as precursors for subsequent etching treatment.

Synthesis of hierarchical porous hollow $FeFe(CN)_6$-100 and $FeFe(CN)_6$-120 nanospheres: Briefly, 35.0 mg $FeFe(CN)_6$-80 and 100 mg PVP were added into 30 ml of 1.0 M HCl solution, which was then kept in a tightly sealed stainless autoclave and heated at 100 °C for 5 h in an electric oven. The stainless autoclave was left to cool down to room temperature. The blue product, $FeFe(CN)_6$-100 nanospheres, was collected via centrifugation and washed thoroughly with ultra-pure water, before drying at 60 °C overnight. $FeFe(CN)_6$-120 nanospheres were obtained in a similar manner by etching treatment at 120 °C.

Synthesis of the $FeFe(CN)_6$@IG

15 mg IG and 75 mg PBAs precursor ($FeFe(CN)_6$-80 or $FeFe(CN)_6$-100 or $FeFe(CN)_6$-120) were ultrasonically dispersed in 30 mL H_2O. After freeze-drying for 48 h, the loose navy blue powders ($FeFe(CN)_6$-80@IG or $FeFe(CN)_6$-100@IG or $FeFe(CN)_6$-120@IG) were obtained.

Materials characterizations

The X-ray diffraction (XRD) patterns were obtained on Rigaku D/Max III diffractometer with CuK radiation, λ=1.5418 Å). The scanning electron microscopy was performed on Verios 460L (FEI, America) scanning electron microscope. The transmission electron microscopy (TEM) was performed on a Tecnai G2 Spirit TWIN (FEI, America). FTIR spectra using KBr pellets were recorded on a PerkinElmer Frontier Mid-IR FTIR spectrometer from 400-4000 cm^{-1}. Raman spectroscopy was performed on a Renishaw inVia spectrometer in the wavenumber range of 400-4000 cm^{-1} using 514.5 nm laser. The surface areas of these samples were determined through N_2 adsorption/desorption isotherms collected at 77 K (Quantachrome iQ-MP gas adsorption analyzer). The surface chemical compositions of these samples were characterized on X-ray photoelectron spectroscopy (XPS, Thermo Scientific ESCALAB 250Xi).

Electrochemical measurements

For electrochemical tests, the working electrodes were prepared with active materials ($FeFe(CN)_6$@IG), acetylene black (AB), and polyvinylidene fluoride (PVDF) at the weight ratio of 80: 10: 10. In the test cells, the lithium serves as the counter and reference electrode, Celgard 2400 membrane was used as the separator. The electrolyte is 1.0M $LiPF_6$ dissolved in a 1: 1: 1 mixture of ethylene carbonate (EC), ethylene methyl carbonate (EMC) and dimethyl carbonate (DMC). The cells were assembled in a glove box filled with high-purity argon. The discharge/charge measurements were conducted at a voltage interval of 0.001 to 3.0 V at room temperature. Electrochemical

impedance spectroscopy (EIS) was taken by using an IM6e electrochemical workstation at 25 °C in the frequency range from 10 kHz to 100 mHz and an AC signal of 5 mV in amplitude as the perturbation. Cyclic voltammetry (CV) tests were performed using a CHI 760E electrochemical workstation at 1 mV s^{-1} between 0.001 and 3.0 V.

Results and discussion

As shown in Figure S2, different morphology of $FeFe(CN)_6$ nanostructures including nanocubes, a mixture of nanocubes and nanospheres, and nanospheres were prepared at 80 °C under similar conditions by varying the concentration of HCl solution from 0.05M to 0.2 M and 0.5 M. To obtain more porous $FeFe(CN)_6$ nanospheres, $FeFe(CN)_6$ nanospheres obtained at 80 °C with the presence of 0.5 M HCl solution were subjected to further heat treatment at higher temperature (100 °C and 120 °C) and concentration of HCl (1.0 M). The morphologies of resultant various $FeFe(CN)_6$ nanospheres were observed under both scanning electron microscopy (SEM) and transmission electron microscope (TEM). The primitive $FeFe(CN)_6$-80 nanospheres precursors are highly uniform with a rather smooth surface and an average size of 250 nm (Figure 1a, 1d and 1g). All diffraction peaks of the precursor in the X-ray diffraction (XRD) pattern (see Figure S3, Supporting Information) could be indexed to typical $FeFe(CN)_6$ (JCPDS Card No. 01-0239).[47] After etchings at different temperature, XRD analysis shows that the crystal phase of the particles was not altered. It should be pointed out here the peak intensities in the XRD pattern increase after 120 °C etching. With the increase of etching temperature, the roughness of the surface became more apparent as shown in Figure 1b and 1c. The sizes of the nanospheres are slightly reduced to ≈230 nm. Energy-dispersive spectroscopy (EDS) mapping (see Figure S4, Supporting Information) indicates the even distribution of Fe, C, and N in the $FeFe(CN)_6$-100 heterostructure. The validity of the etching process could be further confirmed from TEM observations. After etching at 100 °C, the surface of these particles became noticeably rougher (Figure 1e and 1h) while the overall nanospherical shape was retained. Along with this, some large pores were produced upon etching as revealed by much brighter contrast difference throughout the whole particle (Figure 1h). When the etching temperature was increased to 120 °C, the morphology was changed slightly into a flower-like structure (Figure 1f and1i). Figure S5 shows the N_2 adsorption-desorption isotherm curves for $FeFe(CN)_6$-80, $FeFe(CN)_6$-100

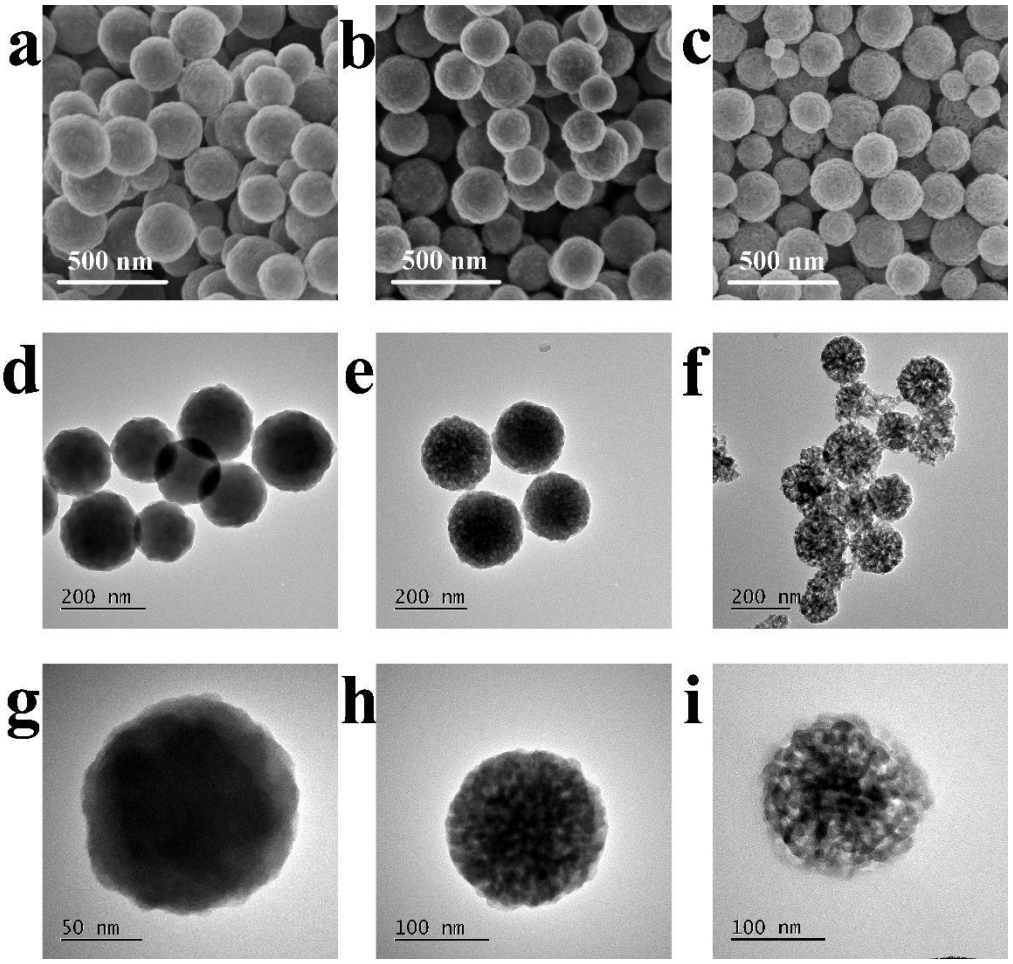

Figure 1 SEM (a-c) and TEM (d-i) images of the $FeFe(CN)_6$-80 (a, d, g), $FeFe(CN)_6$-100 (b, e, h), $FeFe(CN)_6$-120 (c, f, i).

View Article Online
DOI: 10.1039/C8DT05150J

and $FeFe(CN)_6$-120 prepared under different etching temperature (80, 100, and 120 °C). The pristine $FeFe(CN)_6$-80 nanospheres only had a surface area as low as 88.66 $m^2\ g^{-1}$. After etching at 100 °C and 120 °C, the surface areas were increased to 367.76 and 130.50 $m^2\ g^{-1}$ for $FeFe(CN)_6$-100 and $FeFe(CN)_6$-120, respectively. We further calculated the pore volume of these three samples, among which $FeFe(CN)_6$-100 showed the largest pore volume as high as 0.433 $cm^3\ g^{-1}$. On the contrary, pristine $FeFe(CN)_6$-80 and $FeFe(CN)_6$-120 had pore volumes of 0.148 $cm^3\ g^{-1}$ and 0.230 $cm^3\ g^{-1}$, respectively These results indicate that the etching temperature has a significant effect on the degree of etching of $FeFe(CN)_6$ nanospheres.

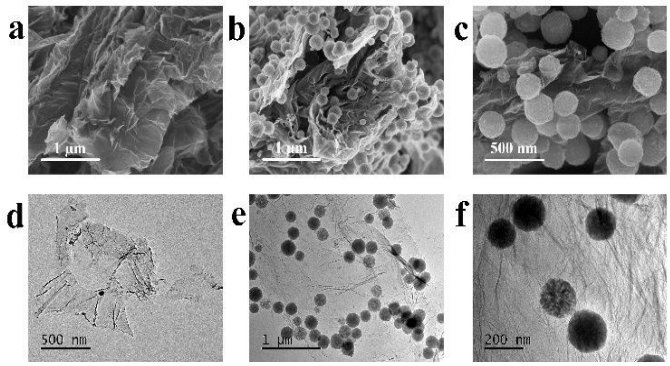

Figure 2 SEM (a-c) and TEM (d-f) images of the IG (a, d) and $FeFe(CN)_6$-100@IG (b, c, e, f).

The morphology of the highly crumpled IG sheets and $FeFe(CN)_6$-100@IG were examined by SEM and TEM. Figure 2a confirms that the IG sheets display a fluffy and corrugated morphology with more wrinkles and folded regions. IG sheets are highly crumpled, maintain their two-dimensional (2D) structure (Figure 2d) and randomly aggregate to form a disordered solid. The IG forms a continuous network with the encapsulation of $FeFe(CN)_6$-100 nanospheres (Figure 2b and 2c). This observation is also consistent with the TEM results. The porous spherical $FeFe(CN)_6$-100 particles reside on the IG layer as revealed by the magnified TEM image (Figure 2e and 2f). Such dispersion could enhance the conductivity and alleviate the volumetric strain of $FeFe(CN)_6$-100 nanospheres, simultaneously. Furthermore, compared with graphene wrapping metal oxide/sulfide composites,[48,49] the plane-to-point intimate contact between layered $FeFe(CN)_6$-100@IG composite forms a highly interconnected conductive network, which is beneficial to increase the electrical conductivity of the whole composite as well as the rate performance.

Figure S6a shows the Raman spectra of the obtained I-doped graphene and $FeFe(CN)_6$-100@IG. I-doped graphene shows two distinct peaks of D band (1357 cm^{-1}) and G band (1588 cm^{-1}) as well as a weak 2D band (2590-3060 cm^{-1}).[46] The D and G band are attributed to the defects in the crystal structure and the sp^2-hyhbrized graphitic structure, respectively. It is calculated that the D/G intensity ratio (I_D/I_G) of the I-doped graphene is about 1.10. Due to the edge distortion and cracking during the doping progress, it is believed that the carbon lattice structure of I-doped graphene is more disordered than primitive graphene.[45] A high I_D/I_G band intensity ratio indicates the existence of large amounts of defects and the occurrence of higher doping of graphene by Iodine atoms .[45] Iodine-doped graphene (IG) could induce the formation of pentaiodide (I_5^-) and triiodide (I_3^-) polyanions, which increase the positive charge density on the graphene through surface charge transfer, thus Iodine-doped graphene (IG) possesses enhanced electrical conductivity.[50] Furthermore, halogen atom-doped graphene can improve the stability and capacity of LIBs because of their excellent electrochemical performance.[51]

The successful application of the $FeFe(CN)_6$@IG as an anode is evident from the excellent electrochemical performance of the LIBs. Figure 3a shows the first four cyclic voltammogram (CV) curves of the $FeFe(CN)_6$-100&IG electrode at room temperature between 0.001 and 3.0 V at a scan rate of 1 mV s^{-1}. The $FeFe(CN)_6$@IG anode displays distinct discharge plateaus at 1.6 V, implying the reduction of Fe^{3+} ions coordinated to C and N atoms along with the Li insertion for charge balance in the $FeFe(CN)_6$ lattice. For the first discharge cycle, a strong peak is observed at 0.45 V, which could be attributed to the side reactions occurred on the solid-electrolyte interphase (SEI) film formed on the electrode surfaces.[39] From the second cycle onwards, the CV curves almost overlapped, indicating the stable and superior reversibility of the $FeFe(CN)_6$-100&IG. The peak at 0.76 V during the second discharge process suggests that the Li^+ is inserted into the $FeFe(CN)_6$ without phase decomposition, which will be discussed in details in following part (Figure S14). Figure 3b shows the discharge/charge profiles of the first 50 cycles for the $FeFe(CN)_6$-100&IG anode at a current density of 100 mA g^{-1} between 0.001 V and 3.0 V. The discharge capacity for the first cycle is as high as 1,819.3 mAh g^{-1}, while its first reversible specific capacity is only 973.5 mAh g^{-1}, resulting in an initial coulombic efficiency of approximately 53.51%. Such dramatic capacity loss is attributed to the formation of SEI film, which is commonly observed in I-doped graphene (see Figure S7) and other atoms doped graphene-based electrodes.[46] In addition, the reduction/oxidation of the high-spin Fe^{II}/Fe^{III} ions connected to the nitrogen could not be fully charged. For PBAs with the formula of $M_x[M(CN)_6]_y$ (M = Fe and Mn), two successive steps Li^+ insertion reactions were proposed for $FeFe(CN)_6$ and the corresponding two redox peaks are at 3.7 and 2.9 V, respectively.[52] Similar scenario was also observed for $MnMn(CN)_6$ as an anode material for aqueous electrolyte battery.[53] Here, the two reaction potentials are near 0.7 V vs. SHE and 0.0 V vs. SHE. In our case, as shown in Figure S8 and Figure S9, there are two discharges as well. The first discharge curve of $FeFe(CN)_6$ in the range of 2.0-1.4 V vs Li/Li^+ could be attributed to the reduction of the high-spin $N-Fe^{3+}/Fe^{2+}$. Since this reduction couple could not be reversely charged in the charging process, it disappears in the following cycles and should be responsible for the capacity reduction (Figure 3a). Further discharges took place in the range of 1.4-0.001 V vs Li/Li^+ correspond to the reduction of Fe^{III} to Fe^{II} and then Fe^{I} coordinated with C≡N- by C atoms (equation 2 and 3) as well Fe^{II} to Fe^{I} coordinated with C≡N- by N atoms (equation 4). Similar mechanism was proposed for the use of Prussian blue analogue, cobalt hexacyanocobaltate, as battery anodes in an organic liquid-carbonate electrolyte.[39]

View Article Online
DOI: 10.1039/C8DT05150J

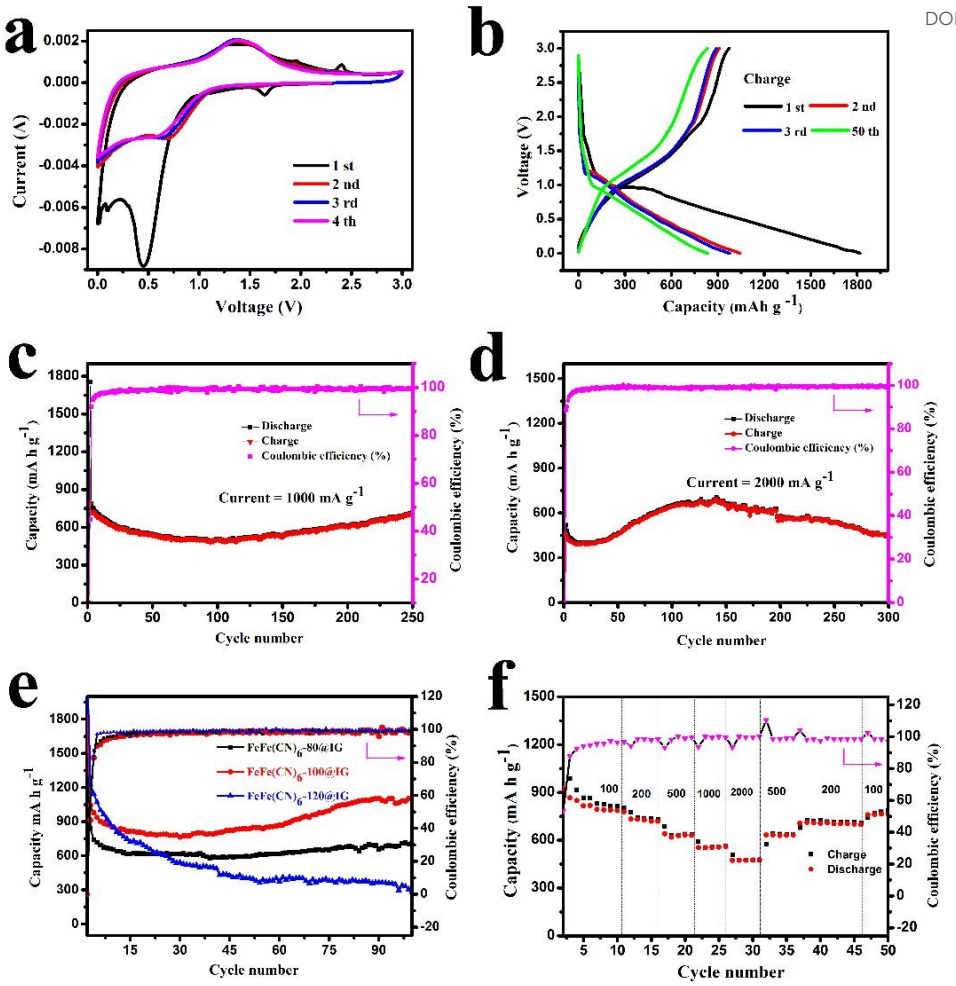

Figure 3 Electrochemical performance of the $FeFe(CN)_6$-100@IG electrode (a-d and f) and comparison of cycling performance of three anodes made from $FeFe(CN)_6$ nanospheres etched under different temperature (e). (a) Cyclic voltammetry curve at 0.001 V s^{-1} scan rate. (b) Galvanostatic charge–discharge profiles at a current density of 100 mA g^{-1}. (c, d) Cycling performances at current densities of 1000 and 2000 mA g^{-1}. (e) Cycling performance of $FeFe(CN)_6$-80@IG, $FeFe(CN)_6$-100@IG, and $FeFe(CN)_6$-120@IG anodes at a current density of 100 mA g^{-1}. (f) Rate performance at different current densities from 100 to 2,000 mA g^{-1}.

Fe^{3+}–C≡N–Fe^{3+} + Li^+ + e^- ⇌ Fe^{3+}–C≡N–$Fe^{2+}Li^+$ (1)

Fe^{3+}–C≡N–$Fe^{2+}Li^+$+ Li^+ + e^- ⇌ Li^+Fe^{2+}–C≡N–Fe^{2+} Li^+ (2)

Li^+Fe^{2+}–C≡N–Fe^{2+} Li^++ Li^+ + e^- ⇌ $2Li^+Fe^+$–C≡N–Fe^{2+} Li^+ (3)

$2Li^+Fe^+$–C≡N–Fe^{2+} Li^++ Li^+ + e^- ⇌ $2Li^+Fe^+$–C≡N–Fe^+ $2Li^+$ (4)

The cycling performance of the $FeFe(CN)_6$-100@IG was evaluated at 1000 mA g^{-1} over a range of 0.001–3.0 V versus Li/Li^+. Electrode prepared from $FeFe(CN)_6$-100@IG maintained discharge capacities of 709.5 mAh g^{-1} after 250 cycles at 1000 mA g^{-1} (Figure 3c) and 448.0 mAh g^{-1} after 300 cycles at 2000 mA g^{-1} (Figure 3d). These results demonstrate the excellent long-term cycling stability of the anode. We further evaluate the electrochemical lithium storage capability of hollow Prussian-blue type $Fe_4[Fe(CN)_6]_3$ with mixed valences of iron cations and contrasting textural properties obtained using similar etching process as potential anode materials for LIBs (Figure S10 and S11). Compared with hollow $Fe_4[Fe(CN)_6]_3$@IG, which shows a cycling performance of 189.7 mAh g^{-1} at 2000 mA after 300 cycles (Figure S12), $FeFe(CN)_6$-100@IG composite shows a superior cycling performance of 448.0 mAh g^{-1} also at 2000 mA after 300 cycles (Figure 3d). Figure 3e shows the comparative cycling performance of three samples at a current rate of 100 mA g^{-1}. Apparently, $FeFe(CN)_6$-100@IG exhibits a significantly improved cyclic capacity retention compared to $FeFe(CN)_6$-80@IG and $FeFe(CN)_6$-120@IG. At the end of 100 charge-discharge cycles, a reversible capacity of 1093.5 mA h g^{-1} can still be retained by $FeFe(CN)_6$-100@IG, while only 710.8 mA h g^{-1} and 305.8 mAh g^{-1} could be retained for $FeFe(CN)_6$-80@IG and $FeFe(CN)_6$-120@IG, respectively. The rapid capacity decay of $FeFe(CN)_6$-120@IG could be attributed to the destruction of the Prussian blue hollow nanospheres. The superior capacity retention given by $FeFe(CN)_6$-100@IG is believed to be originated from its higher porosity created by the controlled etching process, which effectively buffers the volume change during the charge-discharge processes. A significant increase of the specific capacity is observed for the $FeFe(CN)_6$-100@IG from

View Article Online
DOI: 10.1039/C8DT05150J

Active materials	Current density (mA g^{-1})	Initial Capacity	Cycles	Capacity (mAh g^{-1})	Ref.
$Co_3[Co(CN)_6]_2$	20	566.2	5	350	39
PB/graphene foam	100	580	150	514	54
FeP@NC@rGO	1000	760	500	982	55
$Mn_{1.8}Fe_{1.2}O_4$	200	2300	60	827	56
$Mn[Fe(CN)_6]_{0.6667}$	200	1123.7	100	295.7	57
$Mn_xCo_{3-x}O_4$	200	1400	30	733	58
$K_{1-x}Fe_{2+x/3}(CN)_6{\cdot}yH_2O$	8.75	960	50	400	59
$Ti_{0.75}Fe_{0.25}[Fe(CN)_6]_{0.96}$	350	35	50	250	60
$FeFe(CN)_6$@IG	**1000**	**787.3**	**250**	**709.5**	**This work**

Table 1 Comparison of electrochemical performances of reported PBAs and PBAs-derived materials at different current rates.

the 30th to the 100th cycle, which does not occur for the bare $FeFe(CN)_6$ based anode. Such increase in specific capacity could be ascribed to the activation process of I-doped graphene in the anode materials.[46] Figure 3f presents the rate capabilities and the cycle performance of the $FeFe(CN)_6$-100@IG electrode at different current rates. various current densities. When the current density gradually increased from 100 to 200, 500, 1000, and 2,000 mA g^{-1}, the corresponding average discharge capacities decreased from 987, to 804.8, 731.9, 591, and 507.7 mAh g^{-1}, respectively. If the current density was returned to 100 mA g^{-1}, the average discharge capacity was recovered to approximately 758.1 mAh g^{-1}, which indicated a stable cycling performance.

Compared with the reported electrochemical performance of the PBA and PBA-derived materials (Table 1), our results are superior to those of other reported PBA materials for LIBs (Table 1). For example, it was reported that the PB wrapped by graphene foam achieved a capacity of ~514 mAh g^{-1} after 150 cycles at a current density of 100 mA g^{-1}.[54] Whereas single-crystal $Mn[Fe(CN)_6]_{0.6667}{\cdot}nH_2O$ (Mn-PBA) cubes (~600 nm) exhibited a low capacity (~295.7 mAh g^{-1} at 200 mA g^{-1} after 100 cycles).[57] Besides high porosity, two other factors that might be responsible for the outstanding lithium-storage performance of our $FeFe(CN)_6$-100@IG. Firstly, wrinkled graphene sheets wrapping $FeFe(CN)_6$ nanospheres can endure the volumetric change during cycling processes and improve its electrical conductivity. Secondly, our $FeFe(CN)_6$ nanospheres are mainly based on Fe^{3+} instead of a mixture of +2 and +3 metal cations in $M_x[Fe(CN)_6]_y$ (M = Fe, Mn, and Co),[39, 55,57,58] which allows the insertion of more Li^+ into the PB structure upon discharge and therefore a high theoretical capacity could be expected.

To further understand the correlation between the cyclic performance and the structural features of $FeFe(CN)_6$-100@IG, the morphologies of the anode materials under different current density after 100 charge/discharge cycles were observed under SEM. Compared with the fresh electrode $FeFe(CN)_6$-100@IG (Figure S13a and S13b), the $FeFe(CN)_6$-100@IG electrode maintains its integrity, and no crack or pulverization can be observed after 100 cycles at a current density of 100 mA g^{-1} (Figure S13c and S13d). In addition, the $FeFe(CN)_6$-100@IG are uniformly distributed in the composites of polyvinylidene fluoride (PVDF) and acetylene black, further confirming that the unique structure can effectively alleviate the pulverization and prevent particle aggregation and ensure the long-cycle stability. When the charge/discharge current density was set at 1000 mA g^{-1}(Figure S13e and S13f), the intact structure of the electrode after cycling demonstrates that the $FeFe(CN)_6$-100@IG nanostructure can accommodate the stress of volume expansion and prevent the detachment of pulverized Prussain blue during discharge/charge. As a consequence, the rate capability and cycling stability were highly improved. The totally discharged anode after 10 cycles (discharged to 0.001 V at 100 mA g^{-1}) was also characterized under TEM to see the morphology change. From Figure S13g and S13h, we can find that $FeFe(CN)_6$ nanospheres can still bind with I-doped graphene after ten cycles of charge and discharge. The well preserved morphologies of the $FeFe(CN)_6$@IG electrodes suggest that the $FeFe(CN)_6$ nanospheres are very robust material. As we all know, the morphology change on the electrode surface during cycling is responsible for poor cycling stability. This provides evidence for the superior rate performance and enhanced cycling stability in $FeFe(CN)_6$-100@IG electrodes for LIBs.

To unveil the mechanism regulating the cycling stability of $FeFe(CN)_6$ based anode, $FeFe(CN)_6$-100 electrodes were retrieved from the cells after discharging cycle in glovebox under the protection of Ar atmosphere for characterizations. Ex situ XRD patterns (Figure S14) were performed to reveal the phase transition of the $FeFe(CN)_6$-100 nanospheres as a function of potentials during discharge processes. The XRD data of the initial $FeFe(CN)_6$-100 electrode exhibits the most intense reflections of $FeFe(CN)_6$ (at 2 ϑ = 17.3°, 24.7°, 35.2°, 39.4°). It is

View Article Online
DOI: 10.1039/C8DT05150J

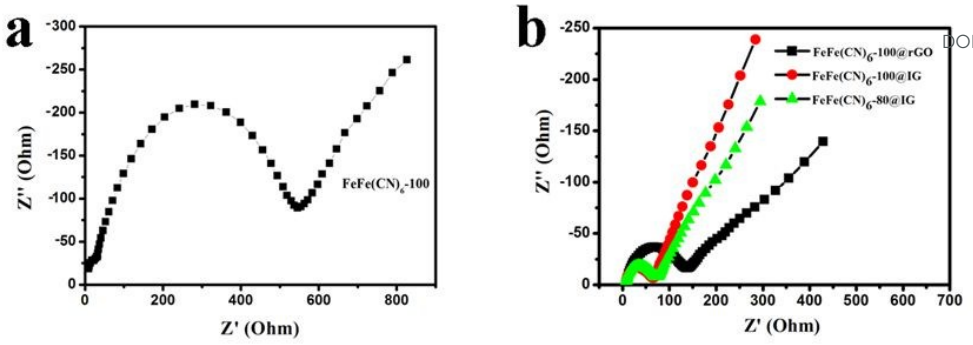

Figure 4 Impedance spectra of $FeFe(CN)_6$-100, $FeFe(CN)_6$-100@rGO, $FeFe(CN)_6$-100@IG and $FeFe(CN)_6$-80@IG.

apparent that no phase transition takes place during the first discharging process to 2.0 V, indicating the insertion of Li^+ ions imposes a negligible impact on the structure of $FeFe(CN)_6$ nanospheres. When the discharge potential of the electrode was reduced to 1.0 V, no obvious structural change could be observed from XRD pattern as Fe^{3+} in the $FeFe(CN)_6$ is expected to be reduced to Fe^{2+} while keeping the structure intact. With the intercalation of Li^+ into the $FeFe(CN)_6$ lattices, the lattice parameters of discharge products were slightly increased through a stepwise intercalation process. Furthermore, once it is fully discharged down to 0.001 V, the intensities of all reflection peaks belonging to the $FeFe(CN)_6$ were dramatically weakened and all peaks were nearly indiscernible as a result of further intercalation of Li^+.

Additional insights into the ion diffusion and charge transfer kinetics during cycling were assessed by electrochemical impedance spectroscopy (EIS). For comparison, we also synthesized a $FeFe(CN)_6$-100@rGO composite and used it also as an anode. According to the EIS analysis (Figure 4), without the presence of IG, $FeFe(CN)_6$-100 has a poor conductivity. Once IG was introduced, both $FeFe(CN)_6$-100@IG and $FeFe(CN)_6$-80@IG electrodes exhibit similar smaller diameter in low frequency region, implying that they have similar electrical resistance. However, at high frequency, $FeFe(CN)_6$-100@IG has a steeper slope which is an indicative of the higher charge transfer and faster reaction rate during the charge/discharge process. The relatively poor electrochemical performance of the $FeFe(CN)_6$-80@IG sample can be mainly attributed to its poor solid nanospheres structure. Even though, both $FeFe(CN)_6$-100@IG and $FeFe(CN)_6$-80@IG show superior electrical conductivity to $FeFe(CN)_6$-100@rGO and necessitate the doping of I into graphene.

Conclusions

In summary, hierarchical porous hollow $FeFe(CN)_6$ nanospheres encapsulated by the I-doped graphene hierarchical network were synthesized via a facile approach. Our experimental results showed that the etching temperature has a significant effect on the degree of etching of $FeFe(CN)_6$ nanospheres. $FeFe(CN)_6$-100 obtained at 100 °C for 5 h in 1.0 M HCl solution possesses high porosity with a specific surface area and pore volume of 367.76 $m^2\ g^{-1}$ and 0.433 $cm^3\ g^{-1}$, respectively. After being integrated with conductive Iodine doped grapheme (IG), the resultant $FeFe(CN)_6$-100@IG was applied as an anode in LIBs. The higher porosity originated from chemical etching process and flexibility provided by the stretchy graphene network within the composite could efficiently alleviate the volume change and allow the rapid transfer of the electrons and lithium ions during the cycling process. As an anode, the as-prepared $FeFe(CN)_6$@IG exhibits improved lithium storage properties, enhanced reversible capacity and robust cyclic stability (709 mAh g^{-1} at the end of 250 cycles under 1000 mA g^{-1}) and quick charge/discharge capability (448.0 mAh g^{-1} at the end of 300 cycles under 2000 mA g^{-1}).

Conflicts of interest

There are no conflicts to declare

Acknowledgements

This work was supported by National Key R&D Program of China (2017YFA0700104), NSFC (21571170 and 21501168) and Tianjin Municipal Science and Technology Commission (17JCZDJC38000).

Notes and references

1 P. Roy, and S. K. Srivastava, J. Mater. Chem. A, 2015, **3**, 2454-2484.
2 G. Derrien, J. Hassoun, S. Panero, and B. Scrosati, Adv. Mater., 2007, **19**, 2336-2340.
3 W. J. Zhang, J. Power Sources, 2011, **196**, 13-24.
4 J. Chen, and F. Cheng, Acc. Chem. Res., 2009, **42**, 713-723.
5 S. Xin, Y. G. Guo, and L. J. Wan, Acc. Chem. Res., 2012, **45**, 1759-1769.
6 T. Ohzuku, Y. Iwakoshi, and K. Sawai, J. Electrochem. Soc., 1993, **140**, 2490-2498.
7 L. Ji, Z. Lin, M. Alcoutlabi, and X. Zhang, Energy Environ. Sci., 2011, **4**, 2682-2699.
8 J. Sanetuntikul, K. Ketpang, and S. Shanmugam, ACS Catal., 2015, **5**, 7321-7327.
9 Z. H. Huang, Y. Song, D. Y. Feng, Z. Sun, X. Sun, and X. X. Liu, ACS Nano, 2018, **12**, 3557-3567.
10 S. Yuan, Y. Zhao, W. Chen, C. Wu, X. Wang, L. Zhang, and Q. Wang, ACS Appl. Mater. Interfaces, 2017, **9**, 21781-21790.

11 W. M. Zhang, J. S. Hu, Y. G. Guo, S. F. Zheng, L. S. Zhong, W. G. Song, and L. J. Wan, Adv. Mater., 2008, **20**, 1160-1165.
12 Y. Chen, H. Xia, L. Lu, and J. Xue, J. Mater. Chem., 2012, **22**, 5006-5012.
13 A. Bhaskar, M. Deepa, M. Ramakrishna, and T. N. Rao, J. Phys. Chem. C, 2014, **118**, 7296-7306.
14 X. W. Lou, D. Deng, J. Y. Lee, and L. A. Archer, Chem. Mater., 2008, **20**, 6562-6566.
15 Y. Zhang, Q. Ma, S. Wang, X. Liu, and L. Li, ACS Nano, 2018, **12**, 4824-4834.
16 G. L. Keegan, D. Aherne, E. Defrancq, Y. K. Gun'ko, and M. Kelly, J. Phys. Chem. C, 2013, **117**, 669-676.
17 D. Tasis, N. Tagmatarchis, A. Bianco, and M. Prato, Chem. Rev., 2006, **106**, 1105-1136.
18 P. Jiang, J. F. Bertone, and V. L. Colvin, Science, 2001, **291**, 453-457.
19 L. Hao, C. Zhu, C. Chen, P. Kang, Y. Hu, W. Fan, and Z. Chen, Synth. Met., 2003, **139**, 391-396.
20 X. Feng, C. Mao, W. G. Yang, W. Hou, and J. J. Zhu, Langmuir, 2006, **22**, 4384-4389.
21 M. K. Park, K. Onishi, J. Locklin, F. Caruso, and R. C. Advincula, Langmuir, 2003, **19**, 8550-8554.
22 Y. Yang, Y. Chu, F. Yang, and Y. Zhang, Mater. Chem. Phys., 2005, **92**, 164-171.
23 L. Yang, Z. Yang, and W. Cao, J. Colloid Interface Sci., 2005, **292**, 503-508.
24 Z. Niu, Z. Yang, Z. Hu, Y. Lu, and C. C. Han, Adv. Funct. Mater., 2003, **13**, 949-954.
25 S. M. arinakos, J. P. Novak, L. C. Brousseau, A. B. House, E. M. Edeki, J. C. Feldhaus, and D. L. Feldheim, J. Am. Chem. Soc., 1999, **121**, 8518-8522.
26 S. M. Marinakos, M. F. Anderson, J. A. Ryan, L. D. Martin, and D. L. Feldheim, Encapsulation, J. Phys. Chem. B, 2001, **105**, 8872-8876.
27 S. M. Marinakos, D. A. Shultz, and D. L. Feldheim, Adv. Mater., 1999, **11**, 34-37.
28 M. Wu, S. A.O 'Neill, L. C. Brousseau, W. P. McConnell, D. A. Shultz, R. J. Linderman, and D. L. Feldheim, Chem. Commun., 2000, **9**, 775-776.
29 S. M. Marinakos, L. C. Brousseau III, A. Jones, and D. L. Feldheim, Chem. Mater., 1998, **10**, 1214-1219.
30 X. Y. Yu, L. Yu, H. B. Wu, and X. W. Lou, Angew. Chem., 2015, **127**, 5421-5425.
31 L. Zhu, X. Q. Liu, H. L. Jiang, and L. B. Sun, Chem. Rev., 2017, **117**, 8129-8176.
32 A. Schoedel, M. Li, D. Li, M. O'Keeffe, and O. M. Yaghi, Chem. Rev., 2016, **116**, 12466-12535.
33 V. J. Witherspoon, J. Xu, and J. A. Reimer, Chem. Rev., 2018, **118**, 10033-10048.
34 H. J. Buser, D. Schwarzenbach, W. Fetter, A. Udi, Inorg. Chem., 1977, **16**, 2704-2710.
35 X. Wu, Y. Luo, M. Sun, J. Qian, Y. Cao, X. Ai, and H. Yang, Nano Energy, 2015, **13**, 117-123.
36 Y. Yang, Z. Lun, G. Xia, F. Zheng, M. He, and Q. Chen, Energy Environ. Sci., 2015, **8**, 3563-3571.
37 J. Nai, and X. W. Lou, Adv. Mater., 2018, 1706825-1706844.
38 L. Shen, Z. Wang, and L. Chen, Chem. Eur. J., 2014, **39**, 12559-12562.
39 P. Nie, L. Shen, H. Luo, B. Ding, G. Xu, J. Wang, and X. Zhang, J. Mater. Chem. A, 2014, **2**, 5852-5857.
40 E. Yoo, J. Kim, E. Hosono, H. S. Zhou, T. Kudo, and I. HonmaLarge, Nano Lett., 2008, **8**, 2277-2282.
41 J. Han, L. Zhang, S. Lee, J. Oh, K. S. Lee, J. R. Potts, J. Ji, X. Zhao, R.S. Ruoff, and S. Park, ACS Nano, 2013, **7**, 19-26.
42 J. Qin, X. Wang, M. Cao, and C. Hu, Chem. Eur. J., 2014, **20**, 9675-9682.
43 C. Zhang, N. Mahmood, H. Yin, F. Liu, and Y. Hou, Adv. Mater., 2013, **25**, 4932-4937.
44 Y. S. Yun, V. D. Le, H. Kim, S. J. Chang, S. J. Baek, S. Park, B.H. Kim, Y. H. Kim, K. Kang, and H. J. Jin, J. Power Sources, 2014, **262**, 79-85.
45 Z. Yao, H. Nie, Z. Yang, X. Zhou, Z. Liu, and S. Huang, Chem. Commun., 2012, **48**, 1027-1029.
46 D. Cai, S. Wang, P. Lian, X. Zhu, D. Li, W. Yang, and H. Wang, Electrochimica Acta, 2013, 90, 492-497.
47 X. Wu, W. Deng, J. Qian, Y. Cao, X. Ai, and H, Yang, *J. Mater. Chem. A*, 2013, **1**, 10130-10134.
48 C. M. Subramaniyam, M. M. Islam, T. Akhter, D. Cardillo, K. Konstantinov, H. K. Liu, and S. X. Dou, RSC Adv., 2016, **6**, 82698-82706.
49 Y. Lv, B. Chena, N. Zhao, C. Shi, C. He, J. Li, and E. Liu, Surf. Sci., 2016, **651**, 10-15.
50 Z. Xiao, Z. Yang, L. Zhang, H. Pan, and R. Wang, ACS Nano, 2017, **11**, 8488-8498.
51 J. Xu, I. Y. Jeon, J. M. Seo, S. Dou, L. Dai, and J. B. Baek, Adv. Mater., 2014, **26**, 7317-7323.
52 X. Wu, M. Shao, C. Wu, J. Qian, Y. Cao, X. Ai, and H. Yang, ACS Appl. Mater. Interfaces, 2016, **8**, 23706-23712.
53 M. Pasta, C. D. Wessells, N. Liu, J. Nelson, M. T. McDowell, R. A. Huggins, M. F. Toney, and Y. Cui, Nat. Commun., 2014, **5**, 3007-3015.
54 M. Zhu, H. Zhou, J. Shao, J. Feng and A. Yuan, J. Alloys Compd., 2018, **749**, 811-817.
55 M. Gao, X. Liu, H. Yang and Y, Yu. Sci. China Chem., 2018, **61**, 1151-1158.
56 F. Zheng, D. Zhu, X. Shi, and Q. Chen, J. Mater. Chem. A, 2015, **3**, 2815-2824.
57 P. Xiong, G. Zeng, L. Zeng, and M. Wei, Dalton Trans., 2015, **44**, 16746-16752.
58 L. Hu, P. Zhang, H. Zhong, X. Zheng, N. Yan, and Q. Chen, Chem. Eur. J., 2012, **18**, 15049-15056.
59 M. J. Piernas-Muñoz, E. Castillo-Martínez, V. Roddatis, M. Armand, and T. Rojo, J. Power Sources, 2014, **271**, 489-496.
60 X. Sun, X. Y. Ji, Y. T. Zhou, Y. Shao, Y. Zang, Z. Y. Wen, and C. H. Chen, J. Power Source, 2016, **314**, 35-38.

View Article Online
DOI: 10.1039/C8DT05150J

Table of Content Entry